

# Experimental signatures of a $\sigma_z\sigma_x$ beam-splitter interaction between a Kerr-cat and transmon qubit

Josiah Cochran<sup>1,\*</sup>, Haley M. Cole<sup>1,†</sup>, Hebah Goderya, Zhuoqun Hao, Yao-Chun Chang, Theo Shaw, Aikaterini Kargioti, and Shyam Shankar<sup>‡</sup>

*Chandra Department of Electrical and Computer Engineering,  
University of Texas at Austin, 2501 Speedway, Austin, TX 78712, USA*  
(Dated: January 8, 2026)

Quantum error correction (QEC) requires ancilla qubits to extract error syndromes from data qubits which store quantum information. However, ancilla errors can propagate back to the data qubits, introducing additional errors and limiting fault-tolerance. In superconducting quantum circuits, Kerr-cat qubits (KCQs), which exhibit strongly biased noise, have been proposed as ancillas to suppress this back-action and enhance QEC performance. Here, we experimentally demonstrate a beamsplitter interaction between a KCQ and a transmon, realizing an effective  $\sigma_z\sigma_x$  coupling that can be employed for parity measurements in QEC protocols. We characterize the interaction across a range of cat sizes and drive amplitudes, confirming the expected scaling of the interaction rate. These results establish a step towards hybrid architectures that combine transmons as data qubits with noise-biased bosonic ancillas, enabling hardware-efficient syndrome extraction and advancing the development of fault-tolerant quantum processors.

## INTRODUCTION

Quantum computing promises to solve problems that are classically intractable, but current hardware is limited by decoherence, gate errors, and measurement infidelity [1]. Achieving fault-tolerant quantum computation requires quantum error correction (QEC), which encodes logical qubits across multiple physical qubits to detect and correct errors without disturbing the encoded information [2]. In the circuit quantum electrodynamics (cQED) platform [3, 4], many QEC demonstrations use large registers of discrete-variable qubits such as the transmon [5–7], incurring significant hardware overhead. Bosonic qubits, which encode quantum information in the infinite-dimensional Hilbert space of a harmonic oscillator, offer a compelling hardware-efficient alternative [8–10]. Examples include cat codes, GKP codes, dual-rail codes, etc. which have demonstrated both passive and active quantum error detection and correction[11–18].

The Kerr-cat qubit (KCQ) is a particular example of a bosonic cat qubit that encodes quantum information in superpositions of coherent states stabilized by Kerr nonlinearity and a two-photon drive [19]. Unlike the related dissipative cat qubit [20, 21], the KCQ is stabilized by Hamiltonian dynamics which enables fast gates while preserving the noise bias intrinsic to cat states. Recent experimental work on the KCQ has demonstrated bit-flip lifetimes of  $\sim 500 \mu\text{s}$ , noise bias  $\sim 100$  and gate fidelities

above 90% [22, 23]. The noise bias can be exploited in tailored QEC codes to improve fault tolerance [24, 25].

The biased noise property of the KCQ has also been theorized to make it an excellent ancilla qubit for QEC when paired with conventional transmons as data qubits [26]. Ancilla qubits are critical in QEC protocols for extracting error syndromes from data qubits [2], but errors on the ancilla can propagate back to the data qubits, degrading error-correction performance [27]. Leveraging a bosonic ancilla with strong noise bias, such as the KCQ, offers a compelling strategy to suppress back-action and enhance fault tolerance [26]. Given that transmons are the most widely adopted qubit in superconducting quantum processors, demonstrating a high-fidelity two-qubit interaction between a transmon and a KCQ is a crucial step toward practical integration of KCQs as ancilla. While prior work has shown similar couplings between a dissipative cat qubit and a transmon[14], as well as a KCQ and an oscillator [28], a biased-noise-compatible interaction between a KCQ and a transmon has not been demonstrated.

In this work, we demonstrate a beamsplitter interaction between a Kerr-cat qubit and a transmon that approximates a  $\hat{\sigma}_z\hat{\sigma}_x$  coupling. Such a coupling may be extended to measure multi-qubit parity observables for QEC, such as in the surface code [26]. The interaction, driven by a single tone at the frequency difference between the two modes, leverages the unique Hamiltonian stabilization dynamics of the KCQ to enable the desired  $\hat{\sigma}_z\hat{\sigma}_x$  coupling. Our results establish a key building block for using the KCQ as a bosonic ancilla for syndrome extraction in fault-tolerant QEC protocols with transmon qubits.

<sup>1</sup> These authors contributed equally to this work.

\* josiah.cochran@austin.utexas.edu

† hmcole@utexas.edu

‡ shyam.shankar@utexas.edu

## SYSTEM DESCRIPTION AND THEORY OF THE BEAM-SPLITTER INTERACTION

The architecture we employ to investigate this interaction is composed of four relevant modes, as shown in Fig. 1b,c. It consists of a mode associated with the KCQ ( $\omega_a$ ), a transmon mode ( $\omega_b$ ) and readout resonator modes associated with the KCQ ( $\omega_{ar}$ ) and transmon ( $\omega_{br}$ ). The KCQ is realized in a driven capacitively-

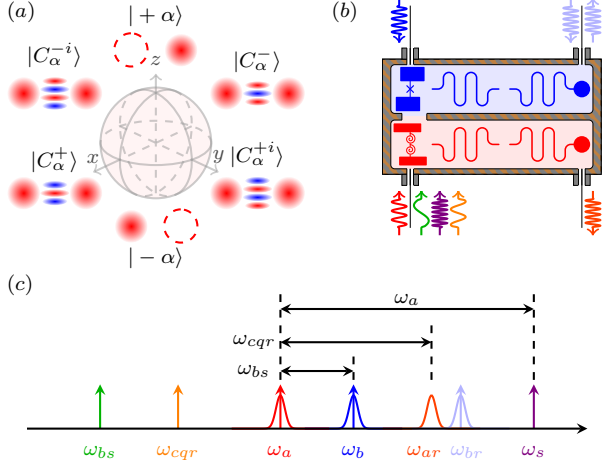


Figure 1. (a) The Bloch sphere of the Kerr-cat with even/odd parity cat states on the  $x$  axis, coherent states on the  $z$  axis and parity-less cat states on the  $y$  axis. (b) Cartoon of the transmon and Kerr-cat with their respective drives color coded according to panel (c). Frequency spectrum of the modes and drives.

shunted Superconducting Nonlinear Asymmetric Inductive eElement (SNAIL) circuit [29]. We refer to the circuit without drive as a SNAILmon in analogy with the transmon. Ignoring the readout resonator and treating the transmon as a two-level system, the relevant terms of the system Hamiltonian can be written as

$$\hat{H}_{\text{sys}}/\hbar = \omega_a \hat{a}^\dagger \hat{a} - K_a \hat{a}^{\dagger 2} \hat{a}^2 + \frac{\omega_b}{2} \hat{\sigma}_z + \frac{\chi_{ab}}{2} \hat{a}^\dagger \hat{a} \hat{\sigma}_z + g_3 (\hat{a} + \hat{a}^\dagger)^2 + \tilde{g}_3 (\hat{a}^{\dagger 2} \hat{\sigma}_- + \hat{a}^2 \hat{\sigma}_+), \quad (1)$$

where  $\hat{a}$  is the annihilation operators for the SNAILmon,  $\hat{\sigma}_z$ ,  $\hat{\sigma}_+$ ,  $\hat{\sigma}_-$  are Pauli operators for the transmon,  $2K_a$  is the SNAILmon anharmonicity,  $\chi_{ab}$  is the dispersive coupling between SNAILmon and transmon and  $g_3$ ,  $\tilde{g}_3$  are terms arising from the third-order nonlinearity of the SNAIL potential.

Similar to previous experiments [19, 28, 30], the KCQ is realized by applying a squeezing drive to the SNAILmon at  $\omega_s = 2\omega_a$ , resulting in an effective KCQ Hamiltonian in the frame rotating at  $\omega_a$ ,  $\hat{H}_{\text{KCQ}}/\hbar = -K_a \hat{a}^{\dagger 2} \hat{a}^2 + \epsilon_2 \hat{a}^{\dagger 2} + \epsilon_2^* \hat{a}^2$ , where  $\epsilon_2$  is the proportional to  $g_3$  and the amplitude of the squeezing drive [19, 26]. The ground states of the KCQ Hamiltonian form a degenerate manifold spanned by even- and odd-parity cat states  $|C_\alpha^\pm\rangle =$

$N_\alpha (|\alpha\rangle \pm |-\alpha\rangle)$  with  $N_\alpha$  being a normalization factor.  $\epsilon_2$  and  $K_a$  set the size of the cat,  $\alpha^2 = \epsilon_2/K_a$  and we assume  $\alpha$  is a real number. This degenerate ground state manifold gives rise to the Bloch sphere, shown in Fig. 1a, with cat states  $|C_\alpha^\pm\rangle$  chosen to lie along the  $x$ -axis and the coherent states  $|\pm\alpha\rangle$  chosen to lie along the  $z$ -axis.

To create the  $\hat{\sigma}_z \hat{\sigma}_x$  interaction, we apply a beam-splitter drive at the difference frequency between the KCQ and transmon ( $\omega_{bs} = \omega_b - \omega_a$ ) and with phase  $\phi$ . The static effective Hamiltonian of the system in the rotating frame of the SNAILmon ( $\omega_a$ ) and transmon ( $\omega_b$ ) becomes

$$\hat{H}/\hbar = \hat{H}_{\text{KCQ}}/\hbar + \frac{\chi_{ab}}{2} \hat{a}^\dagger \hat{a} \hat{\sigma}_z + \tilde{g}_3 \xi (\hat{a}^\dagger \hat{\sigma}_- e^{i\phi} + \hat{a} \hat{\sigma}_+ e^{-i\phi}), \quad (2)$$

where  $\xi$  is the beam-splitter drive amplitude.

Following Ref. [28], we assume the KCQ remains in the ground-state manifold and project into the cat-qubit subspace with the projector  $\mathcal{P}_C = |C_\alpha^+\rangle \langle C_\alpha^+| + |C_\alpha^-\rangle \langle C_\alpha^-|$ . Moreover, through simulations described in Appendix C, we find that the effect of the dispersive shift  $\chi_{ab}$  is negligible. Thus, the effective interaction Hamiltonian for  $\alpha \gg 1$ , is given as

$$\hat{H}_{\text{int}}/\hbar \approx \tilde{g}_3 \xi \alpha \hat{\sigma}_z (\cos(\phi) \hat{\sigma}_x - \sin(\phi) \hat{\sigma}_y), \quad (3)$$

where  $\hat{\sigma}_z$  is an operator on the Kerr-cat Hilbert space shown in Fig. 1a, corresponding to  $|C_\alpha^+\rangle \langle C_\alpha^-| + |C_\alpha^-\rangle \langle C_\alpha^+|$  [28]. In the rest of the text, for all Hamiltonians written with the KCQ projected into the cat-qubit subspace, we write tensor products with the KCQ operators first and transmon operators second. Eqn. 3 shows that the beam-splitter drive realizes the desired  $\hat{\sigma}_z \hat{\sigma}_x$  interaction between KCQ and transmon, with an effective interaction rate  $\Omega = \tilde{g}_3 \xi \alpha$ .

## CIRCUIT REALIZATION AND CHARACTERIZATION

A cartoon of the experimental setup is shown in Fig. 1b, showing the SNAILmon and transmon with their respective readout resonators. The sample package is similar to that of Ref. [31], consisting of two halves machined out of 6061 aluminum and OFHC copper, with the package modes designed to be  $> 1$  GHz above  $\omega_s$ . The package has two 3D cavities which house the transmon and SNAILmon, respectively, with a cut-out between them for capacitive coupling of the qubits, and thus finite  $\chi_{ab}$  and  $\tilde{g}_3$ . Each qubit is fabricated through the Dolan bridge fabrication process on separate sapphire chips. Each chip also has a lithographically defined on-chip readout resonator and Purcell filter. The transmon is designed with a single junction, whereas the SNAILmon is designed with two SNAILs in series to achieve the desired values of  $\omega_a$  and  $K_a$ . Details of the device design and fabrication can be found in Appendix D. Magnetic

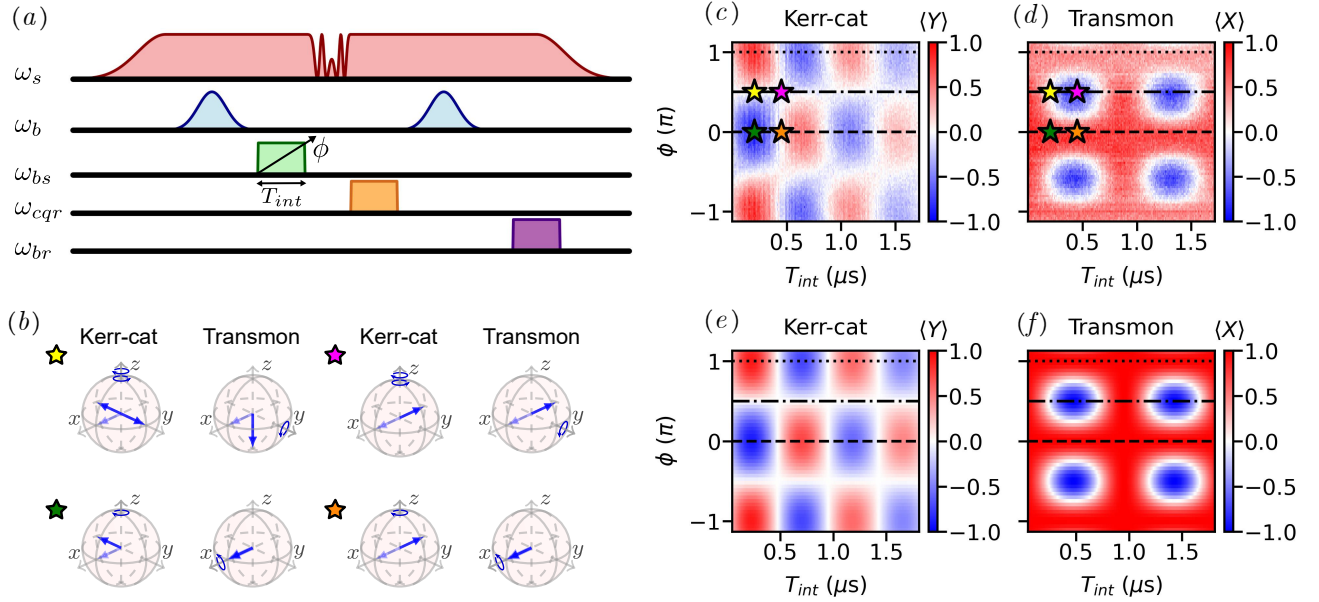


Figure 2. (a) Pulse sequence for measurement of beam-splitter interaction. (b) Bloch spheres that represent the final state (light blue arrows represent the initial state) of the KCQ and transmon for different interaction time and phase (colored stars). (c, d) Experimental and (e, f) simulated signatures of the beam-splitter interaction for varying interaction time and phase for  $\xi = 2.6$ . Colored stars in panel (c, d) correspond to the Bloch spheres in panel (b).

flux is applied to the SNAIL loops via a solenoid magnet, set to an operating flux  $\Phi_{\text{ext}} = 0.33\Phi_0$ , to achieve appreciable  $g_3$  and  $\tilde{g}_3$ . A selected list of Hamiltonian parameters and coherence properties of the qubits at the operating point are given in Tab. I and a complete list is given in Tab. II.

SNAILmon	Value	
<b>Fock basis</b>		
Mode frequency	$\omega_a/2\pi$	5.2 GHz
Relaxation time	$T_1$	40 $\mu$ s
Ramsey decay time	$T_{2R}$	5 $\mu$ s
Operating flux	$\Phi_{\text{ext}}$	0.33 $\Phi_0$
Anharmonicity	$K_a/2\pi$	0.7 MHz
<b>Kerr-cat basis (<math>\alpha = 1.3</math>)</b>		
Coherent state lifetime	$T_\alpha$	25 $\mu$ s
Cat state lifetime	$T_c$	2 $\mu$ s
<b>Transmon</b>	Value	
Mode frequency	$\omega_b/2\pi$	6.7 GHz
Relaxation time	$T_1$	33 $\mu$ s
Ramsey decay time	$T_{2R}$	47 $\mu$ s
Hahn echo decay time	$T_{2E}$	52 $\mu$ s

Table I. **System parameters.** Selected Hamiltonian parameters and coherence times for the transmon, SNAILmon in the Fock basis, and the pumped KCQ in the cat-basis for  $\alpha = 1.3$ .

Stabilization, single-qubit gates and readout of the KCQ are performed with previously demonstrated methods [19, 23, 30, 31]. Control and readout of the qubits was performed with a Xilinx RFSoC with QICK firmware [32, 33], which allowed direct digital synthesis

of the necessary drives with stable phase relationships, obviating the need for complex mixer setups used in previous KCQ demonstrations [19, 23, 30–32]. Details of the experimental setup can be found in Appendix D. The complete procedure for tuning up the  $\sigma_z\sigma_x$  experiment is given in Appendix B.

## SIGNATURES OF $\hat{\sigma}_z\hat{\sigma}_x$ INTERACTION

We demonstrate the beam-splitter interaction between the KCQ and transmon using the pulse sequence shown in Fig. 2a. The KCQ is initialized in  $|\mathcal{C}_\alpha^+\rangle$  state by turning on the squeezing drive,  $\omega_s$  and the transmon is initialized in  $|X\rangle$  with a  $Y_{\pi/2}$  pulse at  $\omega_b$ . Next the beam-splitter interaction is applied with a drive at  $\omega_{bs}$  for varying time and phase. Finally, the KCQ is measured along  $Y$  with a  $X_{\pi/2}$  gate [23] and cat-quadrature readout [19], while the transmon is measured along  $X$  with a  $Y_{\pi/2}$  pulse and dispersive readout.

Experimental measurements and corresponding simulations as a function of the beam-splitter phase ( $\phi$ ) and interaction time ( $T_{int}$ ) are presented in Fig. 2b-f, with the system starting in  $|\mathcal{C}_\alpha^+\rangle|X\rangle$ . From Eq. 3, we see that for  $\phi = 0, \pi$ ,  $\hat{H}_{int} \sim \pm \sigma_z\sigma_x$ . Thus the transmon state  $|X\rangle$  is left unchanged, while the KCQ rotates around  $\pm \sigma_z$ . The dashed ( $\phi = 0$ ) and dotted ( $\phi = \pi$ ) lines in Fig. 2c,d,e,f show the corresponding results, while Fig. 2b shows the final state of the qubits on the Bloch sphere after a quarter (green star) and half (orange star) rotation for  $\phi = 0$ . We see that the transmon remains unchanged as a func-

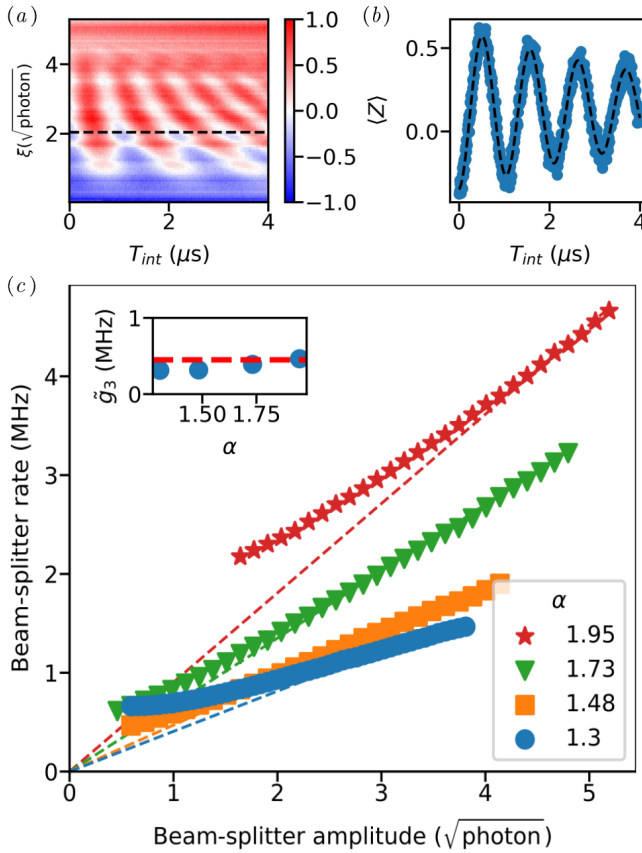


Figure 3. (a) Oscillations of the transmon qubit  $\langle Z \rangle$  observable versus interaction time and drive amplitude  $\xi$  when starting from  $|\psi\rangle = |\mathcal{C}_\alpha^+\rangle |+Z\rangle$ , with  $\alpha = 1.3$ . (b) Data and fit at drive amplitude  $\xi = 2.04$  (dashed line in (a)). (c) Beam-splitter rate versus drive amplitude  $\xi$  for four cat sizes  $\alpha$ . (Inset) Third-order nonlinearity  $\tilde{g}_3$  extracted from experiment (circles) and designed value (dashed red line).

tion of interaction time while the KCQ rotates clockwise for  $\phi = 0$  and counter clockwise for  $\phi = \pi$ . Next, for  $\phi = \pi/2$ , Eq. 3 implies that  $\hat{H}_{int} \sim -\sigma_z \sigma_y$ . Thus, the transmon rotates counter-clockwise in the  $x - z$  plane, as seen along the dotted-dashed line in Fig. 2d,f. At the same time, the KCQ rotates around  $\pm\sigma_z$  with equal weight, implying that  $\langle Y \rangle$  always evaluates to 0 as shown by the dotted-dashed line in Fig. 2c,e.

Next, we studied the interaction speed as a function of beam-splitter amplitude,  $\xi$ , and cat size,  $\alpha$ . The readout contrast and coherence times for the KCQ depends on  $\alpha$ , which makes fits to oscillations of the KCQ  $\langle Y \rangle$  observable to be less reliable as a function of  $\alpha$ . Instead we modified the pulse sequence to observe oscillations of the transmon state during the beam-splitter interaction. The KCQ is again initialized in  $|\mathcal{C}_\alpha^+\rangle$ , while the transmon is initialized in  $|+Z\rangle$ , such that the beam-splitter interaction results in oscillations of the transmon  $\langle Z \rangle$  observable. Fig. 3a shows the transmon  $\langle Z \rangle$  measurement, which oscillates with increasing rate as the beam-splitter

amplitude is increased. The beam-splitter drive amplitude,  $\xi$ , was calibrated in photon number units via a separate Stark shift experiment, described in Appendix A. A representative line cut and fit for amplitude of  $\xi = 2.04$  is shown in Fig. 3b, while Fig. 3c shows the extracted beam-splitter interaction rate,  $\Omega$ , versus  $\xi$ , for several different cat sizes  $\alpha$ . We observe that  $\Omega$  versus  $\xi$  asymptotes to a linear dependence at large enough  $\xi$ . According to Eqn. 3, fitting the slope of this dependence and scaling by  $\alpha$  gives the third-order nonlinearity  $\tilde{g}_3$ . The inset of Fig 3c shows the measured  $\tilde{g}_3$  for various  $\alpha$  and compares to the designed value of 0.45 MHz, showing excellent agreement.

Finally, we extracted the decoherence times experienced by the transmon and KCQ under the beamsplitter interaction. The decay time of the transmon  $\langle X \rangle$  oscillations (shown in Fig 2d, see line cuts in Fig. 7a) is approximately 10 μs, which is consistent with a master equation simulation (described in Appendix C and Fig. 7a). To further experimentally characterize decoherence during the interaction, we fit line cuts from Fig. 3 (where the transmon is now starting in  $|+Z\rangle$ ) and extracted the decay time of the transmon  $\langle Z \rangle$  oscillations versus the cat size and the interaction drive amplitude. The results of this fitting are presented in Fig 7b. In this more comprehensive data set, we observe a decrease in the decay time with increasing beam-splitter drive amplitude, while the effect of cat size remains negligible in the range studied. Moreover, the measured decay time of the transmon under all drive amplitudes, is shorter than the intrinsic  $T_1$  and  $T_{2R}$  of the transmon (Table I). Understanding the cause of this effect is a subject of future study as the ability to perform transmon-KCQ gates without affecting the transmon coherence is crucial to be able to use a KCQ as an ancilla for QEC.

## CONCLUSIONS AND OUTLOOK

In this work, we have experimentally demonstrated a controllable  $\sigma_z \sigma_x$  interaction between a Kerr-cat qubit and a transmon, establishing a key building block for integrating noise-biased bosonic ancillas into error-correction protocols that use transmons as data qubits. Our results confirm that the interaction rate scales in the expected manner with both cat size and drive amplitude across a broad parameter range. Immediate next steps include quantifying the gate fidelity using techniques such as randomized benchmarking and gate-set tomography [23], and investigating the limits on qubit coherence during the interaction. In the medium term, our work opens a promising path toward implementing multi-qubit parity measurements with Kerr-cat ancillas, paving the way for quantum error-correction protocols that mitigate ancilla-induced back-action and enhance overall fault tolerance.

## ACKNOWLEDGEMENTS

The authors thank Dr. Chao Zhou and Prof. Michael Hatridge for providing a custom version of QICK firmware that enabled this experiment. The authors also thank Dr. Nicholas Frattini, and Dr. Benjamin Brock for helpful discussion. This work was supported by the Air Force Office of Scientific Research (Grant No. FA9550-22-1-0203), the Army Research Office (Grant No. W911NF-23-1-0251 and W911NF-23-1-0096) and the Defense Advanced Research Projects Agency (Grant No. HR00112420343). HMC was supported in part by an appointment to the Department of Defense (DOD) Research Participation Program administered by the Oak Ridge Institute for Science and Education (ORISE) through an interagency agreement between the U.S. Department of Energy (DOE) and the DOD. ORISE is managed by Oak Ridge Associated Universities (ORAU) under DOE contract number DE-SC0014664. Sample fabrication was performed in the University of Texas at Austin Microelectronics Research Center, a member of the National Nanotechnology Coordinated Infrastructure (NNCI), which is supported by the National Science Foundation (Grant No. ECCS-2025227). All opinions expressed in this paper are the author's and do not necessarily reflect the policies and views of DOD, DOE, or ORAU/ORISE.

## Appendix A: Beam-splitter drive amplitude calibration

To calibrate beam-splitter drive amplitude  $|\xi|$ , expressed in the RFSoC control as DAC units, to units of  $\sqrt{\text{photons}}$  at the plane of the cavity input port, we perform a Stark shift measurement on the unpumped SNAILmon, i.e. in the Fock basis. When a tone is applied to the SNAILmon, the nonlinear term  $K_a \hat{a}^\dagger \hat{a}^2$  in its Hamiltonian becomes  $K_a |\xi|^2 \hat{a}^\dagger \hat{a}$ , resulting in a frequency shift that is drive amplitude dependent.

Thus, by performing spectroscopy of the SNAILmon with the beam splitter interaction drive applied, as a function of drive amplitude, we extract a conversion factor from DAC units to  $\sqrt{\text{photons}}$  via a fit. Fig. 4 shows the spectroscopy data of the SNAILmon as a function of the beam splitter drive amplitude. The dashed line is a fit to the equation  $\omega_a - K_a(cV)^2$  where  $V$  is the drive amplitude in DAC units (D.U.) and  $c$  is the fitted conversion factor in  $\sqrt{\text{photon}}/\text{D.U.}$  From the fit, we obtain  $c = 6.57 \times 10^{-4} \sqrt{\text{photon}}/\text{D.U.}$

## Appendix B: Procedure for tuning the $\sigma_z \sigma_x$ interaction

The tuning procedure began with continuous-wave (CW) single tone readout spectroscopy, followed by two-

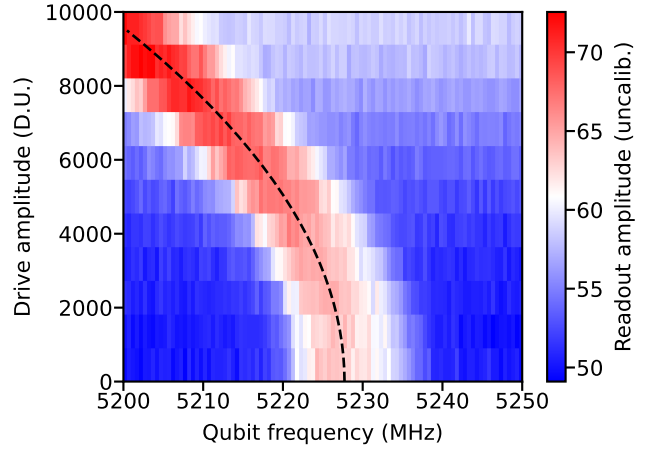


Figure 4. Two tone qubit spectroscopy of the SNAILmon in the Fock-basis with a CW pulse applied at  $\omega_{bs}$  with varying amplitude in DAC units (D.U.).

tone spectroscopy to determine the zero-flux frequency of the SNAILmon. Next, a two tone spectroscopy versus flux was performed, shown in Fig. 5. The flux sweep was

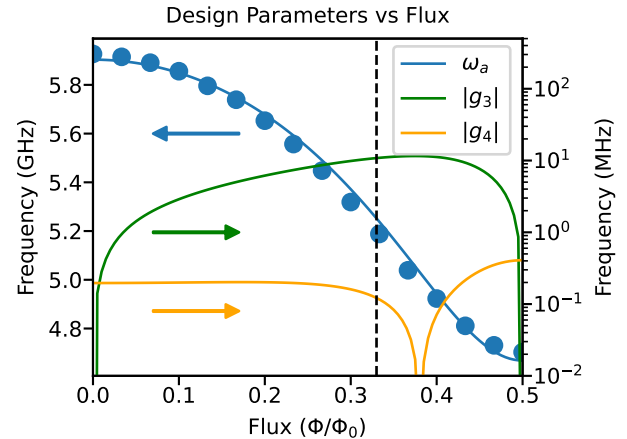


Figure 5. SNAILmon frequency versus flux (blue dots) plotted with a fit (blue line). The extracted nonlinearities  $g_3$  (green),  $g_4$  (orange) are calculated from the fit. Dashed line indicates the chosen operating flux of  $0.33\Phi_0$ .

fit to the SNAILmon model found in Ref. [34], to extract the charging energy  $E_C$  and the linear inductive energy  $E_L$ . Inputs to the fit included the SNAIL asymmetry parameter of 0.1, the number of SNAILs (two) and the measured room temperature resistance values. From the fits we computed  $g_3$  and  $g_4$  as functions of flux, shown in Fig. 5. Since  $g_3$  reaches a maximum beyond the Kerr-free point where  $g_4$  changes sign, we selected an operating flux of  $0.33\Phi_0$  to maximize  $g_3$  while avoiding the region of rapidly varying  $g_4$ .

After setting the operating point, we refined the measurement of the unpumped SNAILmon frequency and its anharmonicity using two-tone spectroscopy with reduc-

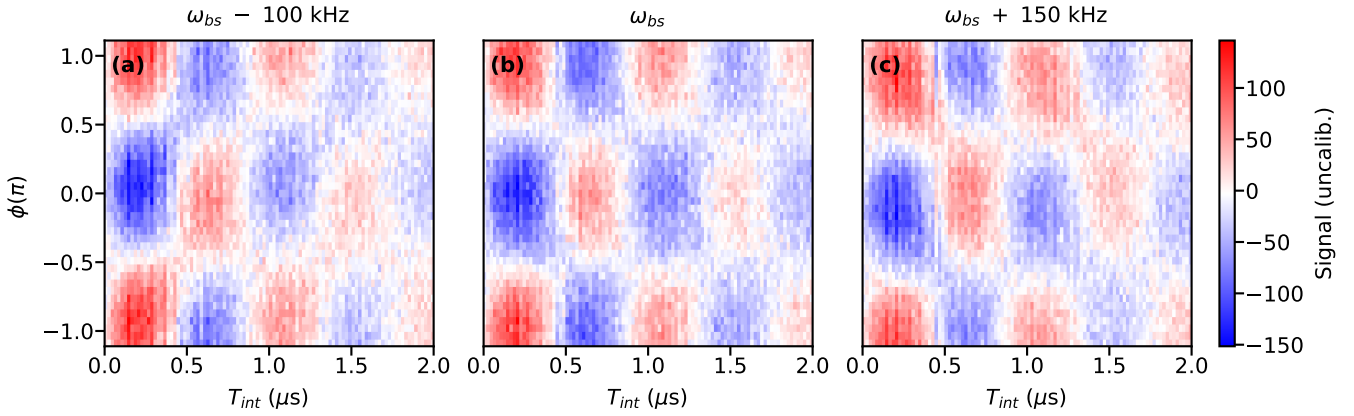


Figure 6. Kerr-cat signal versus interaction time for three cases: (a)  $\omega_{bs}$  detuned by  $-100$  kHz, (b) correctly tuned, (c) detuned by  $+150$  kHz.

ing power. We then characterized coherence times ( $T_1$ ,  $T_2$ ). Next, we calibrated Kerr-cat Rabi oscillations with a Fock basis readout following Grimm et al. [19]. Fitting these oscillations provided the phase offset between the Rabi and squeezing drives on the RFSoC, enabling calibration of the photon number in the cat state as a function of squeezing drive amplitude.

Readout of the Kerr-cat qubit employed the cat-quadrature method [19, 23, 31]. The cat-quadrature readout frequency  $\omega_{cqr}$  was set to  $\omega_a - \omega_{ar}$ , where  $\omega_a$  and  $\omega_{ar}$  were previously determined from spectroscopy. A pulse at  $\omega_{cqr}$  displaced the readout resonator proportionally to the Kerr-cat state. We optimized this pulse by varying its length and amplitude. Implementing cat-quadrature readout required an  $X$ -rotation, which we tuned using the phase-modulation method of Ref. [23]. Once an  $X(\pi/2)$  gate was calibrated, we executed the interaction pulse sequence given in Fig. 2a.

Finally, we fine-tuned the beamsplitter frequency  $\omega_{bs}$ , which must equal  $\omega_b - \omega_a$ . This was achieved by adjusting  $\omega_{bs}$  and recording Kerr-cat oscillations. Fig. 6 shows Kerr-cat oscillations versus interaction time for  $\omega_{bs}$  at the correct frequency and with detunings of  $-100$  kHz and  $+150$  kHz. Negative detuning (panel a) skews the oscillations left, while positive detuning (panel c) skews them right, such that there is no phase with signal amplitude of zero. At the correct frequency (panel b), the response exhibits clear horizontal divisions at  $\pm 90^\circ$  phase, indicating proper tuning.

### Appendix C: Simulations and coherence study

To model the dynamics of the Kerr-cat transmon system, we solved the Lindblad master equation in Qutip [35] with the transmon treated as a two-level system and the Kerr-cat Hilbert space truncated to size  $N = 30$ . The Kerr-cat basis is defined by the states

on the Bloch sphere (Fig. 1a) as  $|\pm X_{KC}\rangle = |\mathcal{C}_\alpha^\pm\rangle = \mathcal{N}_\alpha^\pm (|\alpha\rangle \pm |-\alpha\rangle)$  and  $|\pm Z_{KC}\rangle = |\pm \alpha\rangle$ , where  $\mathcal{N}_\alpha^\pm = 1/\sqrt{2(1 \pm e^{-2|\alpha|^2})}$ . We simulated the Hamiltonian in Eq. 2, without the  $\chi_{ab}$  term, which we separately verified has negligible effect. Thus the simulated Hamiltonian is

$$\hat{H}/\hbar = -K_a \hat{a}^\dagger \hat{a}^2 + \epsilon_2 (\hat{a}^\dagger \hat{a}^2 + \hat{a}^2) + g(t) (\hat{a} \hat{\sigma}_+ e^{i\phi} + \hat{a} \hat{\sigma}_- e^{-i\phi}). \quad (4)$$

$\hat{a}$  is the lowering operator for the Kerr-cat mode.  $g(t) = \tilde{g}_3 \xi f(t)$ , where  $\tilde{g}_3$  is the third-order nonlinearity,  $\xi$  is the interaction drive amplitude and  $f(t)$  is a time-dependent sinusoidal envelope function for turning the interaction on and off. The system evolves according to the master equation

$$\dot{\rho} = -i/\hbar [\hat{H}, \hat{\rho}] + \frac{1}{T_{1,a}} \mathcal{D}[\hat{a}] \hat{\rho} + \frac{1}{T_{2R,a}} \mathcal{D}[\hat{\sigma}_{z,kc}] \hat{\rho} + \frac{1}{T_{1,b}} \mathcal{D}[\hat{\sigma}_-] \hat{\rho} + \frac{1}{T_{2R,b}} \mathcal{D}[\hat{\sigma}_z] \hat{\rho} \quad (5)$$

where  $T_{1,a}$ ,  $T_{2R,a}$ ,  $T_{1,b}$ ,  $T_{2R,b}$  are taken from experimental measurements (Table II).  $\hat{\sigma}_{z,kc}$  is defined as  $|C_\alpha^+\rangle \langle C_\alpha^-| + |C_\alpha^-\rangle \langle C_\alpha^+|$  [28].

### Appendix D: Device fabrication, parameters and experimental setup details

Fig. 2e,f shows the simulated values of the Kerr-cat  $\langle Y \rangle$  and transmon  $\langle X \rangle$  observables for initial Kerr-cat, transmon state  $|+Z_{KC}\rangle |+X\rangle$  for varying interaction time and phase. The comparison with the experimental data in Fig. 2c,d indicates good agreement. Moreover, line cuts of these data and simulations are shown in Fig. 7a, demonstrating good agreement when dephasing and single-photon loss are included.

To further characterize the coherence of the qubits during the interaction, we extracted decay times for the transmon  $\langle Z \rangle$  observable data in Fig. 3. Fig. 7b presents

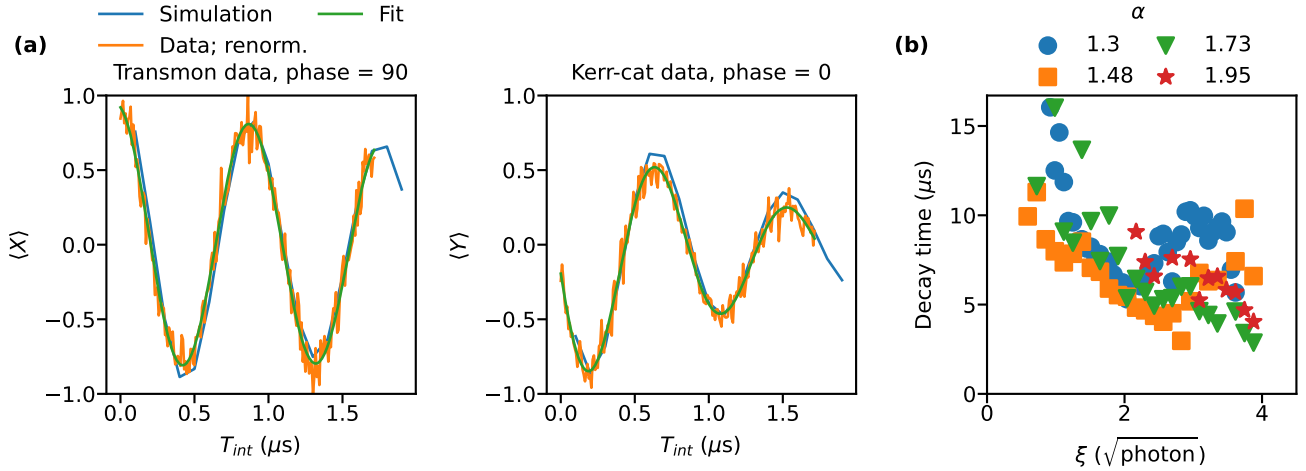


Figure 7. (a) Comparison of experimental line cuts from Fig. 2c,d (orange), fits to the data (green) and simulated line cuts from Fig. 2e,f (blue). The transmon is initialized in  $|+X\rangle$  and the Kerr-cat is initialized in  $|+Z_{KC}\rangle$ . Transmon traces show  $\langle X \rangle$  versus interaction time at a drive phase of  $90^\circ$ , while Kerr-cat traces show  $\langle Y \rangle$  at phase of  $0^\circ$ . (b) Fitted decay time of the transmon oscillations during the interaction, extracted from data in Fig. 3c plotted as a function of interaction drive amplitude  $\xi$  for several values of cat size  $\alpha$ . The qubits are initialized in  $|\psi\rangle = |\mathcal{C}_\alpha^+\rangle |+Z\rangle$

the fitted decay time as a function of interaction drive amplitude,  $\xi$ , for several cat sizes,  $\alpha$ . In this measurement, the transmon is initialized in  $|+Z\rangle$  and observable  $\langle Z \rangle$  was measured, producing oscillations that facilitate accurate fitting of the interaction rate and decay time. We observe the extracted decay times decrease with increasing drive strength, while the dependence on cat size remains negligible within the explored range.

Both chips used in this experiment were fabricated on c-plane sapphire substrates. Wafers were cleaned with N-methyl-2-pyrrolidone (NMP), acetone, and isopropyl alcohol (IPA) followed by a 5-minute dehydration bake at  $175^\circ\text{C}$ . For e-beam lithography, a bilayer resist stack was applied: 650 nm MMA EL13 and 250 nm PMMA A4, baked at  $175^\circ\text{C}$  (1 minute for the first layer, 30 minutes for the bilayer). To mitigate charging during lithography, a 14 nm aluminum anti-charging layer was deposited using an Angstrom e-beam evaporator. Patterns for on-chip readout resonators, Purcell filters, and Josephson junctions were written with a JEOL 8100 e-beam writer. After exposure, the aluminum layer was removed in AD-10 developer (90 s) and then the pattern was developed in 3:1 IPA:H<sub>2</sub>O at  $6^\circ\text{C}$  for 2 minutes, followed by blow dry with nitrogen.

The substrate was then loaded into the evaporator, pumped to below  $2 \times 10^{-7}$  torr, and ion milled with an Ar beam for 90 s. Two aluminum layers are deposited at  $\pm 30^\circ$ , separated by a static oxidation step at 15 torr for 12 minutes with 85:15 Ar:O<sub>2</sub> mixture. After the second aluminum layer deposition, a surface cap oxide was grown at 3 torr for 10 minutes. Lift-off was performed in NMP at  $90^\circ\text{C}$  for 2 hours, followed by rinsing in fresh NMP and

sonication for 1 minute. Devices were then cleaned in acetone, rinsed in IPA, dried with nitrogen, and cleaved using a SYJ-DS100-LD scribe tool.

Measured and simulated device parameters are summarized in Table II, along with the methods used to obtain them taken from Refs. [19, 23, 30]. The experimental setup and wiring diagram are shown in Fig. 8, with component part numbers listed in Table III. A key feature of this setup, compared to previous Kerr-cat experiments [19, 23, 31], is the use of a Xilinx RFSoC in a mixer-less configuration with QICK firmware [32, 33]. A custom firmware version was used to enable reset of the clock phase across all DAC and ADC channels prior to pulse execution [32]. The use of this firmware with phase reset capability was crucial to ensure precise phase alignment for qubit control, readout, and beamsplitter drives during each shot of the experiment.

Parameter	Value	Measurement or estimate method
SNAIL charging energy, $E_C/h$	109 MHz	SNAIL fit
Number of SNAILS	2	Design
SNAIL asymmetry	0.1	Room temperature resistance measurement
SNAIL inductance, $L_J$	0.6 nH	Room temperature resistance measurement
SNAIL frequency at $\Phi/\Phi_0 = 0$	5.93 GHz	Two-tone spectroscopy
SNAIL frequency at $\Phi/\Phi_0 = 0.5$	4.7 GHz	Two-tone spectroscopy
SNAIL operating bias, $\Phi_{\text{ext}}/\Phi_0$	0.33	Design
SNAIL operating frequency, $\omega_a/2\pi$	5.2 GHz	Two-tone spectroscopy
SNAIL cubic nonlinearity, $g_3/2\pi$	11 MHz	Design and SNAIL fit
SNAIL self-Kerr nonlinearity, $K_a/2\pi$	0.7 MHz	Two-tone spectroscopy
Fock basis relaxation time, $T_1$	40 $\mu$ s	Coherence measurement
Fock basis Ramsey decay, $T_{2R}$	5 $\mu$ s	Coherence measurement
Coherent state lifetime, $T_\alpha$ for $\alpha = 1.3$	25 $\mu$ s	Coherence measurement
Cat state lifetime, $T_c$ for $\alpha = 1.3$	2 $\mu$ s	Coherence measurement
Transmon mode frequency, $\omega_b/2\pi$	6.7 GHz	Two-tone spectroscopy
Transmon relaxation time, $T_1$	33 $\mu$ s	Coherence measurement
Transmon Ramsey decay, $T_{2R}$	47 $\mu$ s	Coherence measurement
Transmon Hahn echo decay, $T_{2E}$	52 $\mu$ s	Coherence measurement
SNAIL readout resonator frequency, $\omega_{ar}/2\pi$	8.3 GHz	Single-tone spectroscopy
SNAIL readout resonator linewidth, $\kappa_{ar}/2\pi$	0.1 MHz	Single-tone spectroscopy
Transmon readout resonator frequency, $\omega_{br}/2\pi$	8.56 GHz	Single-tone spectroscopy
Transmon readout resonator linewidth, $\kappa_{br}/2\pi$	2.06 MHz	Single-tone spectroscopy
CQR mode frequency, $\omega_{cqr}/2\pi$	3.1 GHz	Two-tone spectroscopy
Squeezing mode frequency, $\omega_s/2\pi$	10.4 GHz	Two-tone spectroscopy
Beam-splitter mode frequency, $\omega_{bs}/2\pi$	1.5 GHz	Two-tone spectroscopy
Kerr-cat to transmon cross-Kerr, $\chi_{ab}/2\pi$	10 kHz	Simulation

Table II. Summary of device parameters discussed in the main text and appendix, along with the method used to obtain them. Design parameters were determined by Ansys HFSS and pyEPR [36] with corrections described in Ref. [34]. Horizontal lines separate groups of parameters: SNAIL design values, SNAIL parameters at the operating flux, transmon frequency and coherence, readout resonator characteristics, and additional frequencies necessary for the experiment.

Filter	Part no.	Amplifier	Part no.	Balun	Part no.
F1	ZSS2252-100W-S+	A1	ZVA-1W-103+		MABA-011108
F2	ZHSS-11G-S+	A2	ZX60-123LN-S+	<b>Coupler</b>	
F3	ZBSS-3G-S+	A3	ZVE-3W-183+		QMC-CRYOCOUPLER-10
F4	VBFZ-5500-S+	A4	ZVE-3W-83+	<b>Circulator</b>	
F5	ZBSS-10G-S+	A5	ZVA-183-S+	dual junction	LNF-CICIC4 12A S
F6	ZBSS-6G-S+	A6	LNF-LNC4 16B	triple junction	LNF-CHISISC4 12A
F7	6L250-12000				

Table III. Part numbers for all components used in the experiment, listed according to their labels in the wiring diagram shown in Fig. 8.

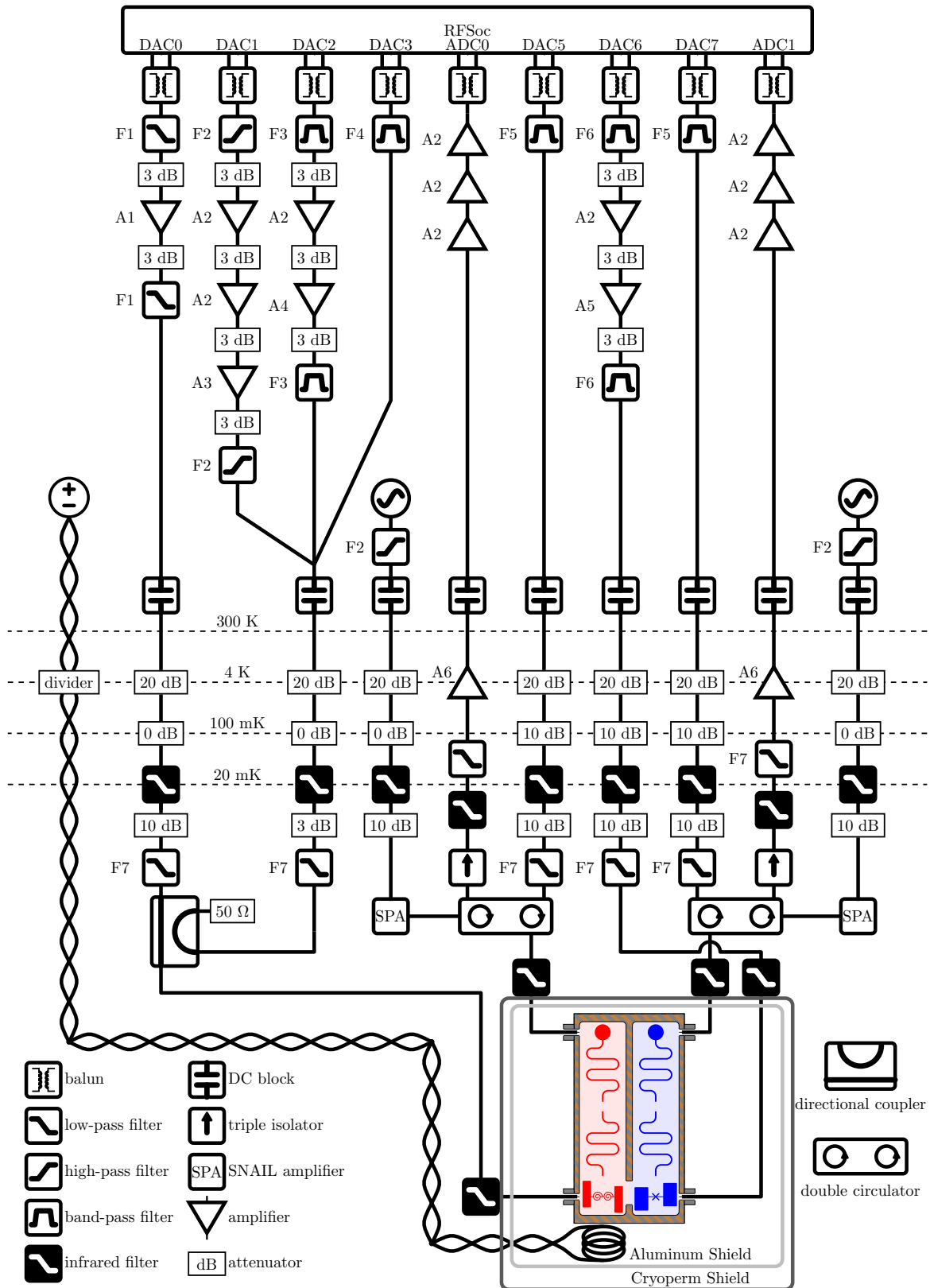


Figure 8. Wiring diagram of the experimental setup, with component definitions referenced in Table III

---

[1] P. Krantz, M. Kjaergaard, F. Yan, T. P. Orlando, S. Gustavsson, and W. D. Oliver, *Applied Physics Reviews* **6**, 021318 (2019).

[2] B. M. Terhal, *Reviews of Modern Physics* **87**, 307 (2015).

[3] A. Blais, R.-S. Huang, A. Wallraff, S. M. Girvin, and R. J. Schoelkopf, *Physical Review A* **69**, 062320 (2004).

[4] A. Blais, A. L. Grimsmo, S. Girvin, and A. Wallraff, *Reviews of Modern Physics* **93**, 025005 (2021).

[5] Y. Zhao, Y. Ye, H.-L. Huang, Y. Zhang, D. Wu, H. Guan, Q. Zhu, Z. Wei, T. He, S. Cao, F. Chen, T.-H. Chung, H. Deng, D. Fan, M. Gong, C. Guo, S. Guo, L. Han, N. Li, S. Li, Y. Li, F. Liang, J. Lin, H. Qian, H. Rong, H. Su, L. Sun, S. Wang, Y. Wu, Y. Xu, C. Ying, J. Yu, C. Zha, K. Zhang, Y.-H. Huo, C.-Y. Lu, C.-Z. Peng, X. Zhu, and J.-W. Pan, *Physical Review Letters* **129**, 030501 (2022).

[6] Google Quantum AI and Collaborators, R. Acharya, D. A. Abanin, L. Aghababaie-Beni, I. Aleiner, T. I. Andersen, M. Ansmann, F. Arute, K. Arya, A. Asfaw, N. Astrakhantsev, J. Atalaya, R. Babbush, D. Bacon, B. Ballard, J. C. Bardin, and et. al., *Nature* **638**, 920 (2025).

[7] S. Krinner, N. Lacroix, A. Remm, A. Di Paolo, E. Genois, C. Leroux, C. Hellings, S. Lazar, F. Swiadek, J. Hermann, G. J. Norris, C. K. Andersen, M. Mller, A. Blais, C. Eichler, and A. Wallraff, *Nature* **605**, 669 (2022).

[8] B. M. Terhal, J. Conrad, and C. Vuillot, *Quantum Science and Technology* **5**, 043001 (2020).

[9] A. Joshi, K. Noh, and Y. Y. Gao, *Quantum Science and Technology* **6**, 033001 (2021).

[10] W. Cai, Y. Ma, W. Wang, C.-L. Zou, and L. Sun, *Fundamental Research* **1**, 50 (2021).

[11] N. Ofek, A. Petrenko, R. Heeres, P. Reinhold, Z. Leghtas, B. Vlastakis, Y. Liu, L. Frunzio, S. M. Girvin, L. Jiang, M. Mirrahimi, M. H. Devoret, and R. J. Schoelkopf, *Demonstrating Quantum Error Correction that Extends the Lifetime of Quantum Information* (2016), version Number: 1.

[12] J. M. Gertler, B. Baker, J. Li, S. Shirol, J. Koch, and C. Wang, *Nature* **590**, 243 (2021).

[13] U. Rglade, A. Bocquet, R. Gautier, J. Cohen, A. Marquet, E. Albertinale, N. Pankratova, M. Halln, F. Rautschke, L.-A. Sellem, P. Rouchon, A. Sarlette, M. Mirrahimi, P. Campagne-Ibarcq, R. Lescanne, S. Jezouin, and Z. Leghtas, *Nature* **629**, 778 (2024), arXiv:2307.06617 [quant-ph].

[14] H. Putterman, K. Noh, C. T. Hann, G. S. MacCabe, S. Aghaeimeibodi, R. N. Patel, M. Lee, W. M. Jones, H. Moradinejad, R. Rodriguez, N. Mahuli, J. Rose, J. C. Owens, H. Levine, E. Rosenfeld, P. Reinhold, L. Moncelsi, J. A. Alcid, N. Alidoust, and et. al., *Nature* **638**, 927 (2025).

[15] V. V. Sivak, A. Eickbusch, B. Royer, S. Singh, I. Tsoutsios, S. Ganjam, A. Miano, B. L. Brock, A. Z. Ding, L. Frunzio, S. M. Girvin, R. J. Schoelkopf, and M. H. Devoret, *Nature* **616**, 50 (2023).

[16] B. L. Brock, S. Singh, A. Eickbusch, V. V. Sivak, A. Z. Ding, L. Frunzio, S. M. Girvin, and M. H. Devoret, *Nature* **641**, 612 (2025).

[17] A. Koottandavida, I. Tsoutsios, A. Kargiotti, C. R. Smith, V. R. Joshi, W. Dai, J. D. Teoh, J. C. Curtis, L. Frunzio, R. J. Schoelkopf, and M. H. Devoret, *Erasure detection of a dual-rail qubit encoded in a double-post superconducting cavity* (2023), arXiv:2311.04423 [quant-ph].

[18] K. S. Chou, T. Shemma, H. McCarrick, T.-C. Chien, J. D. Teoh, P. Winkel, A. Anderson, J. Chen, J. Curtis, S. J. d. Graaf, J. W. O. Garmon, B. Gudlewski, W. D. Kalfus, T. Keen, N. Khedkar, C. U. Lei, G. Liu, P. Lu, Y. Lu, A. Maiti, L. Mastalli-Kelly, N. Mehta, S. O. Mundhada, A. Narla, T. Noh, T. Tsunoda, S. H. Xue, J. O. Yuan, L. Frunzio, J. Aumentado, S. Puri, S. M. Girvin, S. H. Moseley, and R. J. Schoelkopf, *Demonstrating a superconducting dual-rail cavity qubit with erasure-detected logical measurements* (2023), arXiv:2307.03169 [quant-ph].

[19] A. Grimm, N. E. Frattini, S. Puri, S. O. Mundhada, S. Touzard, M. Mirrahimi, S. M. Girvin, S. Shankar, and M. H. Devoret, *Nature* **584**, 205 (2020).

[20] R. Lescanne, M. Villiers, T. Peronnin, A. Sarlette, M. Delbecq, B. Huard, T. Kontos, M. Mirrahimi, and Z. Leghtas, *Nature Physics* **16**, 509 (2020).

[21] C. Berdou, A. Murani, U. Rglade, W. Smith, M. Villiers, J. Palomo, M. Rosticher, A. Denis, P. Morfin, M. Delbecq, T. Kontos, N. Pankratova, F. Rautschke, T. Peronnin, L.-A. Sellem, P. Rouchon, A. Sarlette, M. Mirrahimi, P. Campagne-Ibarcq, S. Jezouin, R. Lescanne, and Z. Leghtas, *PRX Quantum* **4**, 020350 (2023).

[22] N. E. Frattini, R. G. Cortias, J. Venkatraman, X. Xiao, Q. Su, C. U. Lei, B. J. Chapman, V. R. Joshi, S. Girvin, R. J. Schoelkopf, S. Puri, and M. H. Devoret, *Physical Review X* **14**, 031040 (2024).

[23] A. Hajr, B. Qing, K. Wang, G. Koolstra, Z. Pedramrazi, Z. Kang, L. Chen, L. B. Nguyen, C. Jnger, N. Goss, I. Huang, B. Bhandari, N. E. Frattini, S. Puri, J. Dressel, A. N. Jordan, D. I. Santiago, and I. Siddiqi, *Physical Review X* **14**, 041049 (2024).

[24] A. S. Darmawan, B. J. Brown, A. L. Grimsmo, D. K. Tuckett, and S. Puri, *PRX Quantum* **2**, 030345 (2021).

[25] Q. Xu, N. Mannucci, A. Seif, A. Kubica, S. T. Flammia, and L. Jiang, *Physical Review Research* **5**, 013035 (2023).

[26] S. Puri, A. Grimm, P. Campagne-Ibarcq, A. Eickbusch, K. Noh, G. Roberts, L. Jiang, M. Mirrahimi, M. H. Devoret, and S. Girvin, *Physical Review X* **9**, 041009 (2019).

[27] D. S. Wang, A. G. Fowler, A. M. Stephens, and L. C. Hollenberg, *arXiv preprint arXiv:0905.0531* (2009).

[28] A. Z. Ding, B. L. Brock, A. Eickbusch, A. Koottandavida, N. E. Frattini, R. G. Cortinas, V. R. Joshi, S. J. d. Graaf, B. J. Chapman, S. Ganjam, L. Frunzio, R. J. Schoelkopf, and M. H. Devoret, *Quantum Control of an Oscillator with a Kerr-cat Qubit* (2024), arXiv:2407.10940 [quant-ph].

[29] N. E. Frattini, U. Vool, S. Shankar, A. Narla, K. M. Sliwa, and M. H. Devoret, *Applied Physics Letters* **110**, 222603 (2017).

[30] N. E. Frattini, R. G. Cortias, J. Venkatraman, X. Xiao, Q. Su, C. U. Lei, B. J. Chapman, V. R. Joshi, S. M. Girvin, R. J. Schoelkopf, S. Puri, and M. H. Devoret, *Physical Review X* **14**, 10.1103/PhysRevX.14.031040 (2024), arXiv:2209.03934 [quant-ph].

[31] J. Venkatraman, R. G. Cortias, N. E. Frattini, X. Xiao, and M. H. Devoret, *Proceedings of the National Academy of Sciences* **121**, 10.1073/pnas.2311241121 (2024), publisher: Proceedings of the National Academy of Sciences.

[32] C. Ding, M. Di Federico, M. Hatridge, A. Houck,

S. Leger, J. Martinez, C. Miao, D. S. I, L. Stefanazzi, C. Stoughton, S. Sussman, K. Treptow, S. Uemura, N. Wilcer, H. Zhang, C. Zhou, and G. Cancelo, *Physical Review Research* **6**, 013305 (2024).

[33] L. Stefanazzi, K. Treptow, N. Wilcer, C. Stoughton, C. Bradford, S. Uemura, S. Zorzetti, S. Montella, G. Cancelo, S. Sussman, A. Houck, S. Saxena, H. Arnaldi, A. Agrawal, H. Zhang, C. Ding, and D. I. Schuster, *Review of Scientific Instruments* **93**, 044709 (2022).

[34] N. E. Frattini, *Three-Wave Mixing in Superconducting Circuits: Stabilizing Cats with SNAILS*, Ph.D. thesis, Yale University (2021), copyright - Database copyright ProQuest LLC; ProQuest does not claim copyright in the individual underlying works; Last updated - 2023-03-08.

[35] J. Johansson, P. Nation, and F. Nori, *Computer Physics Communications* **183**, 17601772 (2012).

[36] Z. K. Minev, Z. Leghtas, S. O. Mundhada, L. Christakis, I. M. Pop, and M. H. Devoret, *Energy-participation quantization of josephson circuits* (2021), arXiv:2010.00620 [quant-ph].